Cosmology with the pairwise kinematic SZ effect: Calibration and validation using hydrodynamical simulations

Bjoern Soergel[1,★], Alexandro Saro[2,3], Tommaso Giannantonio[2,1], George Efstathiou[1], and Klaus Dolag[2,4]

[1] *Institute of Astronomy & Kavli Institute for Cosmology, University of Cambridge, Madingley Road, Cambridge CB3 0HA, UK*
[2] *Universitäts-Sternwarte, Ludwig-Maximilians-Universität München, Scheinerstr. 1, 81679 München, Germany*
[3] *INAF-Osservatorio Astronomico di Trieste, via G.B. Tiepolo 11, 34131, Trieste, Italy*
[4] *Max-Planck-Institut für Astrophysik, Karl-Schwarzschild Strasse 1, 85748 Garching, Germany*

15 December 2017

ABSTRACT

We study the potential of the kinematic SZ effect as a probe for cosmology, focusing on the pairwise method. The main challenge is disentangling the cosmologically interesting mean pairwise velocity from the cluster optical depth and the associated uncertainties on the baryonic physics in clusters. Furthermore, the pairwise kSZ signal might be affected by internal cluster motions or correlations between velocity and optical depth. We investigate these effects using the *Magneticum* cosmological hydrodynamical simulations, one of the largest simulations of this kind performed to date. We produce tSZ and kSZ maps with an area of $\simeq 1600$ deg^2, and the corresponding cluster catalogues with $M_{500c} \gtrsim 3 \times 10^{13}~h^{-1}M_\odot$ and $z \lesssim 2$. From these data sets we calibrate a scaling relation between the average Compton-y parameter and optical depth. We show that this relation can be used to recover an accurate estimate of the mean pairwise velocity from the kSZ effect, and that this effect can be used as an important probe of cosmology. We demonstrate that the residual systematic effects seen in our analysis are well below the remaining uncertainties on the sub-grid feedback models implemented in hydrodynamical simulations.

Key words: Cosmic background radiation – galaxies: clusters: general – large-scale structure of Universe

1 INTRODUCTION

When passing through a cluster of galaxies, a small fraction of cosmic microwave background (CMB) photons are scattered off electrons in the hot, ionized intra-cluster medium (ICM). This process, known as the Sunyaev-Zel'dovich (SZ) effect, can give rise to both a change in the CMB blackbody temperature as well as a spectral distortion (Sunyaev & Zeldovich 1970, 1972, 1980; see also Birkinshaw 1999; Carlstrom et al. 2002 for reviews). While the underlying physical process, the scattering of CMB photons off moving electrons, is the same, the SZ signal is usually broken down into two separate contributions: the *thermal* and *kinematic* SZ effects.

The *thermal* SZ (tSZ) signal is caused by the high random velocities of the electrons in the hot intra-cluster medium, giving rise to a characteristic spectral distortion to the CMB blackbody. Over the past decade, the tSZ effect has become a well-established tool for blind cluster finding in CMB surveys (e.g. Bleem et al. 2015; Hasselfield et al. 2013; Planck Collaboration 2016d), as well as for determining the thermal properties of the ICM in stacked obser-

vations (e.g. Afshordi et al. 2007; Diego & Partridge 2010; Plagge et al. 2010; Planck Collaboration 2011, 2013a,b; Hajian et al. 2013; Soergel et al. 2017; Saro et al. 2017; Erler et al. 2017).

On the other hand, the *kinematic* SZ (kSZ) effect is a result of the bulk motion of the entire cluster, leading to a Doppler shift in the CMB temperature while preserving its blackbody spectrum. This signal offers significant potential for constraints on both astrophysics and cosmology (e.g. Rephaeli & Lahav 1991; Haehnelt & Tegmark 1996; Diaferio et al. 2000; Aghanim et al. 2001; Bhattacharya & Kosowsky 2007). Because of its small amplitude (the ratio of kSZ to tSZ is v$/c \times (k_B T/m_e c^2)^{-1} \simeq 0.1$ for typical clusters) and the lack of a distinctive frequency signature, the kSZ effect has been significantly harder to detect than its thermal counterpart. Nonetheless, it can be extracted using a differential statistic probing the mean relative momentum of the cluster sample (Hand et al. 2012). Applying this *pairwise* estimator to CMB data from the Atacama Cosmology Telescope (ACT, Swetz et al. 2011) and spectroscopic galaxy data from the Baryon Oscillation Spectroscopic Survey (BOSS, Ahn et al. 2012), Hand et al. (2012) obtained the first detection of the kSZ effect.

Subsequently, Planck Collaboration (2016a) reported a de-

★ E-mail: bsoergel@ast.cam.ac.uk

tection obtained with the same estimator. Soergel et al. (2016) demonstrated that this technique can also be used with photometric galaxy cluster catalogues, leading to a detection using data from the Dark Energy Survey (DES, The Dark Energy Survey Collaboration 2005; Dark Energy Survey Collaboration 2016) and the South Pole Telescope (SPT, Lueker et al. 2010). In De Bernardis et al. (2017), the original analysis by Hand et al. (2012) was updated to include more recent ACT and BOSS data; they also detected the expected imprint of redshift-space distortions on the kSZ signal (Sugiyama et al. 2017b). Recently Calafut et al. (2017) and Li et al. (2017) reported further measurements (albeit at low-significance) by combining *Planck* data with various SDSS-based galaxy and cluster samples, and BOSS data, respectively. Furthermore, Sugiyama et al. (2017a) obtained a detection from *Planck* and BOSS data using a Fourier-space version of the pairwise estimator.

There are also alternative statistical approaches: on the one hand it is possible to correlate a CMB map with a reconstructed velocity field (Li et al. 2014); this has led to detections from both *Planck* and ACT data (Planck Collaboration 2016a and Schaan et al. 2016, respectively). The measurements of the *Planck* analysis were used by Ma et al. (2017) to simultaneously constrain optical depth and velocity bias of the used galaxy sample. Hill et al. (2016) and Ferraro et al. (2016) measured the kSZ imprint on the cross-correlation of a squared CMB map with a tracer of the projected density field. Planck Collaboration (2017) reported a detection based on an increased variance in the observed CMB temperature at the positions of clusters. Finally, there have also been kSZ measurements with high-resolution multi-frequency observations of individual clusters (e.g. Sayers et al. 2013).

All these analyses, both with the pairwise and alternative techniques, are close to the detection threshold, with reported significances in the $\simeq 2-4\sigma$ range. However, with ongoing and upcoming CMB and large-scale structure surveys, detection significances will increase dramatically (e.g. Keisler & Schmidt 2013; Flender et al. 2016; Alonso et al. 2016; Ferraro et al. 2016). Therefore the kSZ effect is expected to mature rapidly into a cosmological probe. In this paper, we test whether the kSZ signal can be used as an accurate probe of cosmology. We focus on the pairwise statistic because it is a robust detection method with a well-studied astrophysical and cosmological sensitivity. In particular, previous works (Soergel et al. 2016; De Bernardis et al. 2017; Flender et al. 2017) have assumed the simple relation

$$T_{\mathrm{pkSZ}}(r, z) \simeq \overline{\tau} \frac{T_{\mathrm{CMB}}}{c} v_{12}(r, z) \tag{1}$$

between the pairwise kSZ signal T_{pkSZ} and the average optical depth $\overline{\tau}$ and mean pairwise velocity v_{12} of the cluster sample. In a fixed cosmology, and given a prescription for the halo bias, $v_{12}(r, z)$ can be calculated (e.g. Sheth et al. 2001). Therefore $\overline{\tau}$ can be determined with a simple template fit; its variation with aperture or filtering scale is then a probe of the gas fraction and density profile of the clusters (Hernández-Monteagudo et al. 2015; Soergel et al. 2016; Sugiyama et al. 2017a).

If, on the other hand, we want to obtain cosmological constraints from the pairwise kSZ measurement, this argument needs to be turned around: we require a *prediction* for the optical depth to reconstruct an estimate of the mean pairwise velocity (Dolag & Sunyaev 2013; Battaglia 2016; Flender et al. 2017). This measurement then constrains the parameter combination $Hf\sigma_8^2$ (Keisler & Schmidt 2013; Sugiyama et al. 2017a), where H is the Hubble parameter, f is the linear growth rate of density perturbations,

and σ_8 is their amplitude averaged over a sphere of 8 h^{-1}Mpc.[1] Therefore the pairwise kSZ signal can be used to constrain various aspects of cosmology, including dark energy or modified gravity (Bhattacharya & Kosowsky 2007, 2008; Keisler & Schmidt 2013; Mueller et al. 2015b) or massive neutrinos (Mueller et al. 2015a).

In this paper we test whether the assumption of eq. 1 in fact holds at the precision required to extract cosmology from the high-significance pairwise kSZ measurements that are expected from future surveys. Internal cluster motions, bulk rotation, or relative velocities between dark matter and gas can introduce significant scatter in the relation between halo peculiar velocity and observed kSZ signal (Cooray & Chen 2002; Chluba & Mannheim 2002; Nagai et al. 2003; Diaferio et al. 2005). These effects could also cause a bias to the observed pairwise kSZ signal (Dolag & Sunyaev 2013), for example if internal motions are correlated with the environment or bulk motion of a cluster. The approximation of eq. 1 could also break down if there is a non-negligible degree of correlation between velocity and optical depth of haloes. We show how these two potential biases propagate into the observed pairwise kSZ signal in Sec. 3.5 below.

Modelling these effects requires hydrodynamical simulations with sufficient resolution to resolve internal cluster dynamics. Furthermore, simulations of the pairwise kSZ signal require a large box size to capture the large-scale motions of clusters on $\gtrsim 100$ Mpc scales. The combination of these two requirements has made these simulations prohibitively expensive until recently. In this work, we use the *Magneticum* simulation suite[2], which contains amongst others one of the largest hydrodynamical simulations performed to date. This enables us to create simulated cluster catalogues and tSZ and kSZ maps that are well matched to upcoming CMB and large-scale structure surveys, both in terms of sky coverage and mass and redshift range. With these, we are able to test the potential of the pairwise kSZ signal as a cosmological probe in detail.

Our paper is structured as follows: In Sec. 2 we briefly review the theory of both SZ effects and describe the simulation and the production of cluster catalogues and SZ maps. Our analysis methods for predicting the optical depth and measuring the pairwise kSZ signal are detailed in Sec. 3. In Sec. 4 we show the resulting measurement of the mean pairwise velocity and compare it to the true value obtained directly from the halo catalogue. We further discuss the implications for the pairwise kSZ signal as a cosmological probe, before concluding in Sec. 5.

2   THEORY AND SIMULATIONS

2.1   SZ effects

2.1.1   Kinematic SZ

The kSZ effect preserves the blackbody spectrum of the CMB, but imparts a Doppler shift given by (Sunyaev & Zeldovich 1980)

$$\frac{\Delta T_{\mathrm{kSZ}}}{T_{\mathrm{CMB}}} = -\sigma_T \int \mathrm{d}l\, n_e(\mathbf{r}) \frac{\hat{\mathbf{r}} \cdot \mathbf{v}_e(\mathbf{r})}{c} \simeq -\tau \frac{\mathrm{v}_{\mathrm{los}}}{c}, \tag{2}$$

where n_e and $\mathbf{v}_e$ are the number density and peculiar velocity of electrons in a cluster at direction $\hat{\mathbf{r}}$ and σ_T is the Thomson cross section. If internal motions of the cluster gas are negligible (which

---

[1] When redshift-space effects are included, there are additional corrections, and the pairwise kSZ signal needs to be decomposed into multipoles (Sugiyama et al. 2017a).

[2] http://www.magneticum.org/

might not be a good approximation; see above), the kSZ signal reduces to the product of cluster line-of-sight velocity and the optical depth

$$\tau = \int \mathrm{d}l \, n_e(\mathbf{r}) \sigma_T \, . \tag{3}$$

2.1.2 Thermal SZ

The tSZ effect, on the other hand, induces a spectral distortion of the microwave background. In the non-relativistic limit it is given by (Sunyaev & Zeldovich 1970)

$$\frac{\Delta T_{\mathrm{tSZ}}}{T_{\mathrm{CMB}}} = y f(x) \quad \text{with} \quad f(x) = x \coth(x/2) - 4 \, . \tag{4}$$

Here $x = h\nu/(k_B T_{\mathrm{CMB}})$ is a dimensionless frequency, and the Compton-y parameter is given by

$$y = \int \mathrm{d}l \, n_e(\mathbf{r}) \, \sigma_T \, \frac{k_B T_e(\mathbf{r})}{m_e c^2} \, . \tag{5}$$

While relativistic corrections are non-negligible for massive clusters with electron temperature $k_B T_e \gtrsim 10$ keV (e.g. Carlstrom et al. 2002), these objects are rare. The bulk of the pairwise kSZ signal is coming from much lower masses, so neglecting relativistic corrections to the tSZ signal does not introduce a significant bias into our analysis.

2.2 Magneticum simulations

Here we only describe the simulations briefly; for a more detailed description we refer to previous work using these simulations (e.g. Dolag et al. 2016; Bocquet et al. 2016; Gupta et al. 2017). The *Magneticum* simulations are a set of state-of-the-art, cosmological hydrodynamical simulations of different cosmological volumes with different resolutions performed with an improved version of GADGET3 (Springel 2005; Beck et al. 2016). They follow a standard ΛCDM cosmology with parameters close to the best-fitting values from WMAP7 (Komatsu et al. 2011), i.e. a matter density $\Omega_m = 0.272$, baryon density $\Omega_b = 0.046$ and a Hubble constant of $H_0 = 70.4$ km s^{-1} Mpc^{-1}. The spectral index of the primordial power spectrum is $n_s = 0.963$, whereas the normalization of the present-day power spectrum is given by $\sigma_8 = 0.809$.

These simulations follow a wide range of physical processes (see Hirschmann et al. 2014; Teklu et al. 2015 for details) which are important for studying the formation of active galactic nuclei (AGN), galaxies, and galaxy clusters. The simulation set covers a huge dynamical range following the same underlying treatment of the physical processes controlling galaxy formation, thereby allowing to reproduce the properties of the large-scale, intra-galactic and intra-cluster medium (Dolag et al. 2016; Gupta et al. 2017; Remus et al. 2017a), as well as the detailed properties of galaxies including morphological classifications and internal properties (Teklu et al. 2015; Remus et al. 2017b; Teklu et al. 2017). This also includes the distribution of different metal species within galaxies and galaxy clusters (Dolag et al. 2017), and the properties of the AGN population within the simulations (Hirschmann et al. 2014; Steinborn et al. 2016).

Here we focus on the largest box ('Box0') with size $L = 2688 \, h^{-1}$Mpc and 2×4536^3 particles (see also Bocquet et al. 2016; Pollina et al. 2017), making it the largest cosmological hydrodynamical simulation performed to date. Such a large box size

Redshift slice	z_{tab}	width [cMpc]	depth [cMpc]
$0.00 < z < 0.07$	0.001	101	288
$0.07 < z < 0.21$	0.138	406	585
$0.21 < z < 0.38$	0.294	826	615
$0.38 < z < 0.57$	0.472	1264	636
$0.57 < z < 0.78$	0.673	1713	645
$0.78 < z < 1.04$	0.903	2171	664
$1.04 < z < 1.32$	1.181	2631	652
$1.32 < z < 1.59$	1.480	3042	521
$1.59 < z < 1.84$	1.709	3375	429
$1.84 < z < 2.15$	1.983	3689	469

Table 1. Redshift slices used for the creation of the lightcone.

is essential for our purposes as the pairwise kSZ signal only vanishes at scales $r \gtrsim 300$ Mpc; furthermore large cluster samples are required to analyse the kSZ signal.

We identify halos using a friends-of-friends algorithm with linking length $b = 0.16$. For the identified halos we then compute their properties – like spherical overdensity masses – using the SUBFIND algorithm (Springel et al. 2001; Dolag et al. 2009); see Bocquet et al. (2016) and the discussion therein for the obtained halo mass function. We note that even the smallest halos we consider ($M_{500c} \gtrsim 3 \times 10^{13} \, h^{-1} M_\odot$) are still resolved by $\gtrsim 2000$ dark matter particles and the associated number of gas and star particles.

2.3 SZ maps

Ideally, one would create the SZ maps by placing an observer at one corner of the simulation box. One would then solve the lightcone equation for every particle, interpolating their positions between the snapshots (as e.g. in Flender et al. 2016). Only gas particles within the lightcone would then contribute to the SZ map. This approach is, however, not feasible for hydrodynamical simulations, as the gas properties cannot be interpolated safely between snapshots (one would miss shocks, for example). Furthermore, this problem will be exacerbated if the stored snapshots are relatively far apart, as it is necessarily the case for such a large simulation as the one considered here. Producing the maps on the fly without relying on snapshots, on the other hand, would add significantly to the computational complexity of the simulation.

We therefore approximate the full lightcone by a series of redshift slices with $\Delta z \simeq 0.2$, making use of the SMAC code (Dolag et al. 2005).[3] For every slice, we take a region of appropriate width and depth from the simulation box at the corresponding redshift z_{tab} (see Table 1). We then calculate the kSZ and tSZ signal from the slices via eqs. 2 and 5 by projecting along the z-axis of the simulation box. The maps for the full lightcone are then simply given by the co-addition of the signals from the individual slices. We show the final kSZ and tSZ maps in Fig. 1.

The map size in this approach is determined by the size of the simulation box and the highest desired redshift. For $z_{\mathrm{max}} \simeq 2$, this yields a map size of $\simeq 40$ deg, corresponding to an area of $\simeq 1600$ deg^2.[4] We note that this is sufficiently large to match the sky coverage of current and future analyses correlating high-resolution CMB and large-scale structure data. For reference, the

---

[3] http://wwwmpa.mpa-garching.mpg.de/~kdolag/Smac/

[4] Larger sky coverages can, of course, be achieved if z_{max} is reduced. In addition, one could project the box along different axes; the duplication of structures caused by this approach would be minimal.
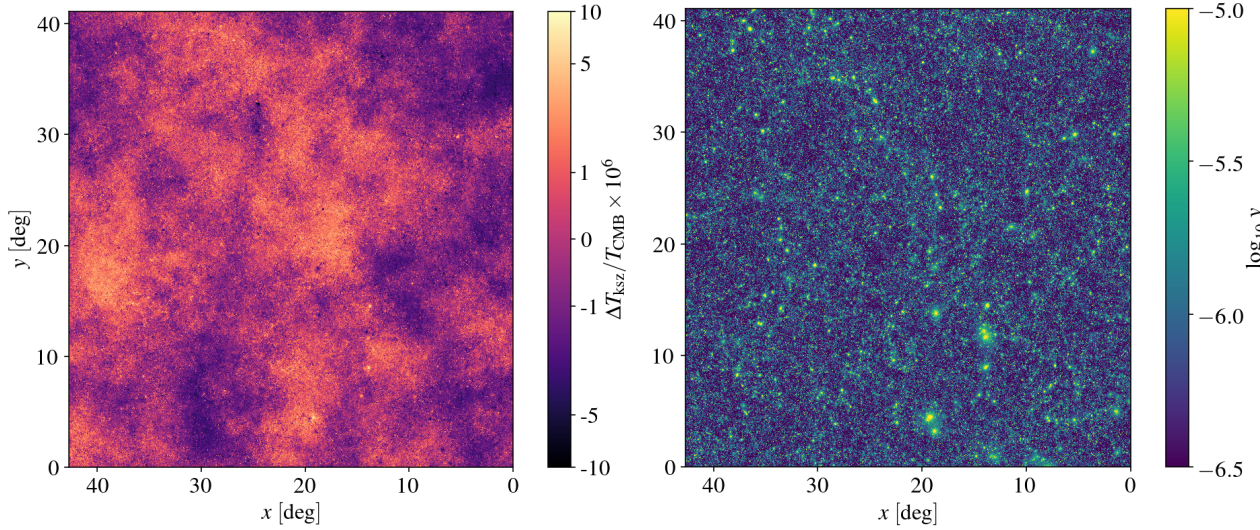
Figure 1. SZ maps from the *Magneticum* simulations: We show on the left the kSZ signal, where we have used an arcsinh(..) colour mapping to increase the dynamic range, while at the same time preserving the sign of the kSZ. For the tSZ signal in the right panel we show the logarithm of the Compton-y parameter.

effective overlapping sky area between DES Year 1 and SPT is around 1,200 deg^2 (Soergel et al. 2016).

As part of the validation of our map pipeline, we compute the power spectrum of the kSZ and tSZ map in the range $\ell = [100, 10\,000]$ and show them in Fig. 2. Dolag et al. (2016) have previously compared SZ power spectra from the second-largest *Magneticum* box ('Box1', $L = 896\ h^{-1}$Mpc) to observations. They found the predicted tSZ power spectrum to be in good agreement with *Planck* ($\ell \lesssim 1000$), but higher than measured by ACT (Dunkley et al. 2013) and SPT (George et al. 2015) on smaller scales. Here we observe the same for the largest *Magneticum* box.

It is worth noting that especially the high-ℓ tSZ power spectrum is sensitive to the sub-grid physics of the simulation, and particularly to the strength of AGN feedback (e.g. McCarthy et al. 2014). The same holds true for the kSZ power spectrum; see e.g. Park et al. (2017) for a recent study using the Illustris simulation. Given that we are focussing on a single sub-grid model for the feedback processes here, there is inevitably a systematic uncertainty associated with our predictions; see Sec. 4.3 below for a further discussion.

2.4 Mass and redshift selection

For the main analysis we select clusters by imposing a lower mass limit of $M_{500c} > 3 \times 10^{13}\ h^{-1} M_\odot$, leaving around 65,000 clusters in our sample. During the post-processing of the simulation data we have also calculated a variety of other observationally relevant quantities, such as X-ray luminosity, stellar mass, and integrated SZ signal. The distribution of these quantities (all within R_{500c}), and how they correlate with each other, is shown in Fig. 3. It would also be possible to select clusters by various mass proxies, such as L_X, M_*, or Y_{SZ}. Therefore we can, in principle, create mock catalogues for clusters selected in the X-ray, optical or via their SZ signature; in this case, the scatter in the mass-observable relations would cause a Malmquist-type bias in the selected catalogue (see Fig. 3). A detailed mock-up of observational cluster selection with all its subtleties is, however, beyond the scope of this paper.

We further divide the clusters in redshift bins which coincide with the redshift limits of the slices used for the SZ map produc-
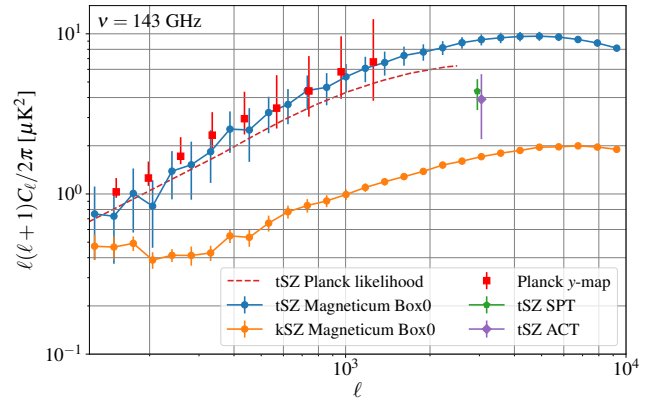

Figure 2. SZ power spectra: We show here the kSZ and tSZ power spectra from the *Magneticum* simulation, where the error bars are estimated by splitting the map into 5×5 rectangular sub-patches. For the tSZ component, we compare to the power spectrum of the *Planck y*-map (Planck Collaboration 2016c), the best-fitting tSZ template from the *Planck* likelihood (Planck Collaboration 2016b), and to measurements of the tSZ power at $\ell = 3000$ from ACT (Dunkley et al. 2013) and SPT (George et al. 2015). It is worth noting that the latter two measurements used tSZ templates that differ in shape from our simulation results. This will likely have an impact on the level of agreement between ACT/SPT and the simulated SZ power spectrum (see also Fig. 6 in Dolag et al. 2016). In all cases, we have scaled the measurements to a frequency of 143 GHz.

tion. This is to ensure that there is no bias to the pairwise kSZ signal on large scales. Such a bias could arise because our way of slicing the simulation box does not preserve the large-scale correlations between adjacent slices. The typical comoving thickness of a redshift slice is $\simeq 600$ Mpc, whereas the largest scales at which we probe the pairwise kSZ signal are 300 Mpc. Given that these scales only differ by a factor of two, the pairwise kSZ signal at the largest scales would be biased low because by construction we have removed the correlation between cluster pairs from different slices.
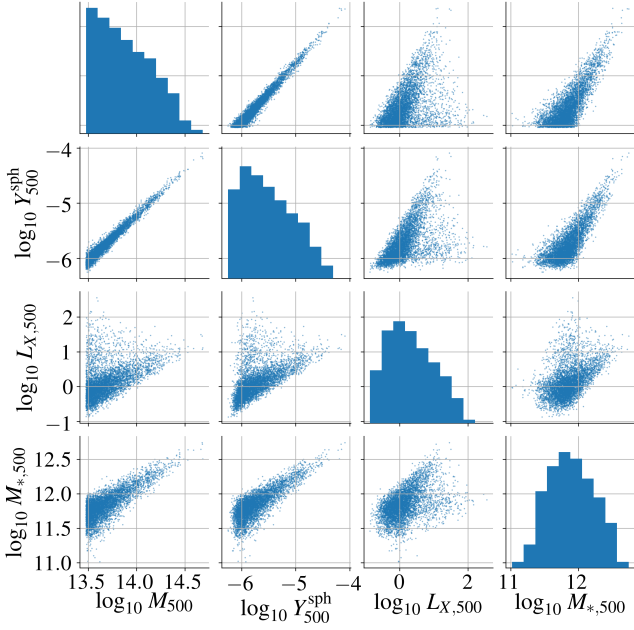
Figure 3. Selection of the cluster properties calculated during the simulation post-processing: On the diagonals we show the distribution of M_{500} $[h^{-1}M_\odot]$, the integrated Compton-y parameter Y_{500} [Mpc^2], X-ray luminosity $L_{X,500}$ [10^{44} erg/s] and stellar mass $M_{*,500}$ [$h^{-1}M_\odot$]. The off-diagonal panels show the correlations between the respective quantities. The lower mass limit was set to $M_{500c} > 3 \times 10^{13}$ $h^{-1}M_\odot$.

By only considering the signal in the appropriate redshift bins, we preclude such a bias.

We focus on the five redshift bins between $z = 0.21$ and $z = 1.32$. The excluded two lowest redshift bins ($z < 0.21$) have few clusters because of their small volume. Similarly, the three highest bins ($z > 1.32$) would provide poor statistics because clusters are rare objects at these high redshifts. The remaining redshift range $0.21 < z < 1.32$ is a good match to cluster samples expected from current and future surveys and contains around 54,000 clusters with $M_{500c} > 3 \times 10^{13}$ $h^{-1}M_\odot$. We show the mass distribution in these five bins in Fig. 4.

3 ANALYSIS METHODS

3.1 Scaling relations for the optical depth

The existence of a scaling relation between optical depth and tSZ signal was first pointed out by Diaferio et al. (2000), who found that $y \propto \tau^2$ was a good empirical fit to the results of their N-body simulations and semi-analytic modelling. Nagai et al. (2003) suggested reconstructing τ from the observed tSZ signal and mean electron temperature. However, this would require the density-weighted average T_e, which is not observable. Simulating one cluster at high resolution, they found that when using the emission-weighted temperature as measured from X-ray observations (T_X) instead, this leads to a significant bias ($\simeq 20\%$) on the recovered optical depth and therefore the peculiar velocity. Using a sample of $\simeq 100$ massive clusters from a cosmological box, Diaferio et al. (2005) obtained similar conclusions, with estimated biases on the peculiar velocity ranging between 20 and 50%. These results were confirmed by Dolag & Sunyaev (2013) using more modern simulations. Fur-
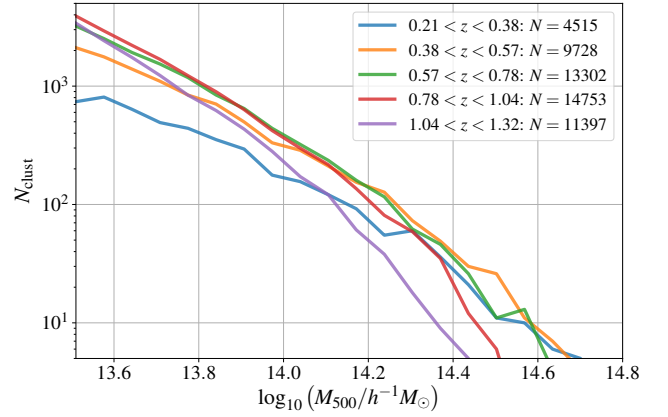

Figure 4. Mass distribution in the five redshift bins. Note that we plot the absolute number of clusters and not their comoving number density. The crossing of the distributions is a result of the combination of cluster growth and volume.

thermore, they found that this bias also propagates into the pairwise measurement: in their case the predicted τ-values had to be reduced by $\simeq 30\%$ to match the pairwise kSZ signal as measured from the same simulation. They also noted that, especially in massive systems, internal motions can contribute a non-negligible extra kSZ signal.

Battaglia (2016, B16 hereafter) used hydrodynamical simulations to calibrate a scaling relation between the optical depth and the Compton-y parameter measured within the same aperture. This has the obvious advantage that no additional observational data are required: the tSZ signal and therefore y can be measured from the same CMB survey as the kSZ. B16 found a tight scaling relation with $\alpha \equiv \mathrm{d}\ln\tau/\mathrm{d}\ln y \simeq 0.5$ for clusters with $M \gtrsim 10^{14} M_\odot$ when averaged within fixed apertures between 1.3′ and 3.9′. De Bernardis et al. (2017) compared the optical depth predicted from the B16 scaling relation to their result obtained with a pairwise kSZ template fit, finding acceptable agreement within the large uncertainties of their measurement. Alonso et al. (2016) derived an analytic model for the y-τ relation. Based on the pressure profile of Arnaud et al. (2010) and the assumption of hydrostatic equilibrium they predict $\alpha \simeq 0.4$ when averaged within R_{500}. However, this approach does not take into account non-thermal pressure support, which can make up a non-negligible part of the total pressure in galaxy clusters (e.g. Battaglia et al. 2012; Nelson et al. 2014).

On the other hand, Flender et al. (2017) calibrated a semi-analytic model for $\tau(M)$ on a compilation of high-resolution X-ray observations of in total $\simeq 160$ clusters. Here the advantage is that one does not have to rely on hydrodynamical simulations with uncertain feedback models. However, the calibrated model for the optical depth is only accurate if the clusters with high-resolution data are representative of the full population, both in terms of mass and redshift range and further properties (e.g. cool-core vs. non-cool-core clusters). Furthermore, the cluster mass is not a direct observable. When applying the $\tau(M)$ relation to a real cluster sample, any uncertainty in the mass-observable relation or in the estimate of hydrostatic mass bias will directly propagate into the prediction for τ.

With these various options to predict the optical depth at hand, the question arises whether we can indeed compress the complex baryonic physics in galaxy clusters into a single number and use it

to extract cosmology from future high-significance kSZ detections. Here we therefore investigate whether a scaling relation for the optical depth can be used to recover an unbiased estimate of the mean pairwise velocity from future high-significance measurements of the pairwise kSZ signal. A flow chart summarizing the analysis steps involved in this comparison is given in Fig. 10 below. We focus on the y-τ relation, but we expect that similar conclusions can be drawn for alternative ways of predicting the optical depth. When calibrating the y-τ relation, we extend the work of B16 to significantly lower masses and higher redshifts, and also point out some important subtleties in the calibration of this relation. Throughout, the guiding principle is to produce a relation that can readily be applied to measurements of the pairwise kSZ signal from real data.

3.2 Map filtering

The observationally relevant quantities are the cylindrical Compton-y parameter and optical depth integrated within an aperture θ_A. We measure these directly from the tSZ and kSZ maps produced from the simulation output as described in Sec. 2.3. To facilitate the application of our scaling relation to real (beam-convolved) CMB data, we have convolved our kSZ and tSZ maps with a Gaussian beam with FWHM = $1.2'$, which is representative of high resolution CMB experiments like ACT and SPT. A more detailed discussion of the impact of the instrumental beam on the calibration of the scaling relation is given in Appendix A.

We then estimate the SZ signal of a cluster centred at position $\hat{\mathbf{n}}_0$ as

$$T_{\text{filt}}(\hat{\mathbf{n}}_0) = \int d^2\hat{\mathbf{n}}\, T(\hat{\mathbf{n}}) W(|\hat{\mathbf{n}} - \hat{\mathbf{n}}_0|) \,, \tag{6}$$

where $T(\hat{\mathbf{n}})$ is the tSZ or kSZ map, respectively. The simplest possible choice is an average within the given aperture θ_A, that is

$$W_{\text{avg}}(\theta) = \frac{1}{\pi\theta_A^2} \times \begin{cases} 1, & \text{if } \theta < \theta_A \\ 0, & \text{if } \theta > \theta_A \end{cases} \,. \tag{7}$$

While this approach is sufficient for simulated tSZ- or kSZ-only maps, it is not well-suited for the application to real CMB data where the primary anisotropies on larger scales dominate the signal. For the main analysis we therefore use an aperture photometry (AP) filter given by

$$W_{\text{AP}}(\theta) = \frac{1}{\pi\theta_A^2} \times \begin{cases} 1, & \text{if } \theta < \theta_A \\ -1, & \text{if } \theta_A < \theta < \sqrt{2}\theta_A \\ 0, & \text{if } \theta > \sqrt{2}\theta_A \end{cases} \,. \tag{8}$$

The normalization constant ensures that this filter returns the average tSZ (or kSZ) signal within the aperture θ_A, but corrected for contributions from larger scales.[5]

The convolution of eq. 6 can be rewritten as a Fourier space filtering with $T_{\text{filt}}(\boldsymbol{\ell}) = \tilde{W}(\ell\theta_A)T(\boldsymbol{\ell})$. There are analytic expressions for the Fourier transforms of these filters given by

$$\tilde{W}_{\text{avg}}(\ell\theta_A) = \frac{2}{\ell\theta_A}J_1(\ell\theta_A) \tag{9}$$

$$\tilde{W}_{\text{AP}}(\ell\theta_A) = \frac{2}{\ell\theta_A}\left[2J_1(\ell\theta_A) - \sqrt{2}J_1(\sqrt{2}\ell\theta_A)\right] \,, \tag{10}$$

respectively. Here ℓ is the modulus of the 2D wavenumber $\boldsymbol{\ell}$, and

---

[5] The AP filter also efficiently removes scatter caused by the large-scale features in the kSZ map (see Fig. 1), which are caused by structures in the low-redshift slices of the simulation.
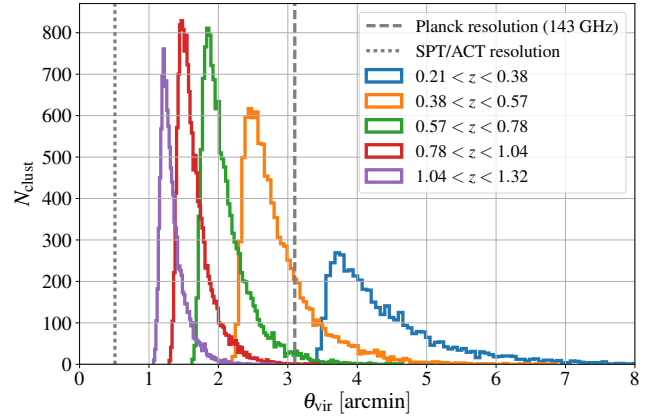

Figure 5. Angular size of the clusters: We show the distribution of θ_{vir} for the five redshift bins considered in the analysis. We have also indicated the the instrumental resolution of various experiments. Specifically, we show $\sigma_{\text{beam}} = \text{FWHM}/\sqrt{8\ln 2}$ and have used FWHM = $7.3'$ for *Planck* (143 GHz) and FWHM = $1.2'$ for SPT/ACT.

J_n denotes a Bessel function of the first kind. As a consistency check for our pipeline, we have implemented and compared both the direct integration in pixel space and the Fourier space filtering. While the Fourier space filtering is efficient in the case of a fixed aperture, it become computationally more expensive if an adaptive aperture is used.

The typical cluster size in our sample varies from $\theta_{500} \simeq 4'$ at $M_{500c} \simeq 4 \times 10^{14}\ h^{-1}M_\odot$ and $z \simeq 0.3$ to $\theta_{500} \simeq 0.7'$ at $M_{500c} \simeq 4 \times 10^{13}\ h^{-1}M_\odot$ and $z \simeq 1.3$. A fixed angular aperture therefore probes different fractions of the cluster for a high-mass/low-z object than for a low-mass/high-z one. Furthermore, the kSZ and tSZ signals have a different dependence on the angular distance from the cluster centre: the kSZ measures $\int dl\, n_e$, whereas the tSZ measures $\int dl\, n_e T_e$, causing the latter to fall off more quickly towards the outskirts.

For both of these reasons we use an adaptive aperture in our analysis. In particular, we use the projected virial radius of the cluster, $\theta_{\text{vir}} \equiv R_{\text{vir}}/d_A$, where d_A is the angular diameter distance. The virial radius is given by

$$R_{\text{vir}} = R_{500}\left(\frac{500 M_{\text{vir}}}{\Delta_{\text{vir}}(z)M_{500}}\right)^{1/3} \,, \tag{11}$$

with $\Delta_{\text{vir}}(z) = 18\pi^2 + 82\tilde{x} - 39\tilde{x}^2$, $\tilde{x} = \Omega(z) - 1$, and $\Omega(z) = \Omega_m(1+z)^3/E^2(z)$ (Bryan & Norman 1998). This choice largely, but not entirely, avoids subtracting part of the signal from the outskirts in the aperture photometry filtering (see Sec. 3.3 and Appendix B below for a more detailed discussion). Furthermore, using the virial radius as an aperture minimizes the scatter in the relation between kSZ signal and halo bulk velocity (Nagai et al. 2003). We show the distribution of angular radii for the five redshift bins in Fig. 5, and compare it to the angular resolution of *Planck* and ground-based high-resolution CMB experiments (SPT, ACT). While most clusters at $z \gtrsim 0.4$ would be unresolved at the *Planck* resolution, they are well resolved with SPT and ACT.

For real data θ_{vir} will of course not readily be available. The average radius of a cluster at a certain redshift can, however, be predicted given a mass-observable relation (e.g. Saro et al. 2015; Simet et al. 2017; Melchior et al. 2017). We have verified that our results do not change significantly if we bin our clusters by their
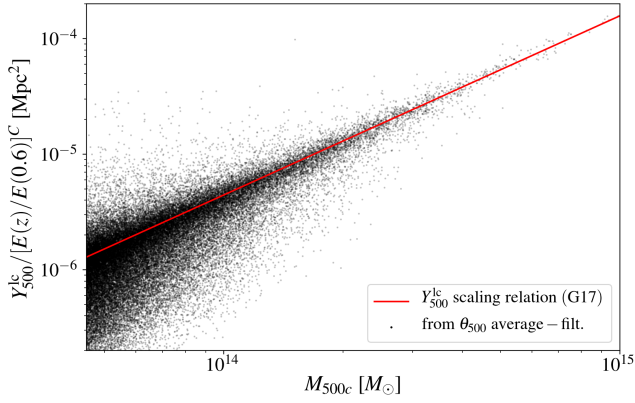
Figure 6. Y-M relation: We show here the Y_{500}^{lc} values obtained by applying the average filter with $\theta_A = \theta_{500}$ to the y-map. For comparison, we show in red the scaling relation fit by Gupta et al. (2017) using a smaller *Magneticum* box and clusters with $M_{500} > 10^{14} \, M_\odot$ ($Y_{500}^{lc} \propto M_{500}^{1.55}$, redshift dependence $C = 0.24$).

angular size and use the average radius within a bin as an aperture. In other words, as long as the mass-observable relation is on average unbiased, we do not require knowledge of the true angular size for every object.

To summarise, our AP filter returns a model-independent estimate for the average tSZ (kSZ) signal of any given cluster. We note that a matched filter (e.g. Haehnelt & Tegmark 1996) could slightly increase the S/N, but it would require assuming a specific cluster profile. Furthermore, tSZ and kSZ have different angular dependencies (see eqs. 2-5), so a single matched filter would not be optimal for both signals relevant to our analysis. For these reasons we use the more model-independent aperture photometry approach.

3.3 y and τ estimates

3.3.1   Measuring y

The observed tSZ signal receives a lightcone contribution from other objects along the same line of sight. As a test for our pipeline, we first measure the integrated cylindrical tSZ signal within θ_{500} including the lightcone contribution, and compare to the results that Gupta et al. (2017) obtained from a smaller ($L = 896 \, h^{-1}$Mpc) box of the *Magneticum* suite and for clusters with $M_{500} > 10^{14} \, M_\odot$. For this purpose, we apply the average filter from eq. 7 to the Compton-y map produced from the simulations. The integrated signal is then given by

$$Y_{500}^{lc} = \langle y \rangle_{\theta_{500}} \times \pi (\theta_{500} d_A)^2, \tag{12}$$

where we denote the Compton-y parameter averaged within an aperture A as $\langle y \rangle_A$ (not to be confused with the average over the cluster sample denoted by $\overline{y}$). We find excellent agreement between the two estimates, as shown in Fig. 6. We further note that the Y-M scaling relation extends to masses well below $10^{14} \, M_\odot$ (down to where it was fitted), albeit with increasing scatter towards low masses.

We then proceed to measure the signal within the virial radius, $\langle y \rangle_{vir}$, using the AP filter of eq. 8. We reiterate that the same AP procedure can be applied to observational data, as the AP also efficiently removes any fluctuations on scales larger than the aperture (such as the primary CMB). Therefore we use $\langle y \rangle_{vir}$ when calibrating the y-τ relation.
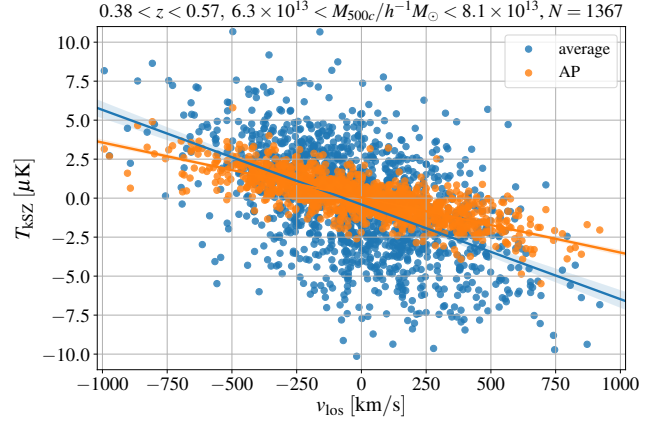
Figure 7. Determination of the optical depth: Here we show the tight relation between the AP-filtered T_{kSZ} and v_{los} for one redshift slice and mass bin. The optical depth is determined from the slope of the relation using eq. 2. For illustration purposes we also show the same procedure using the average signal of every cluster (i.e. without background subtraction), which leads to significantly larger scatter and a slightly steeper slope (see Appendix B).

3.3.2   Measuring τ

In B16 the optical depth of individual clusters was measured by projecting the electron density in the entire $165 \, h^{-1}$Mpc simulation box along one axis, and then averaging within a fixed aperture. This approach works well enough for a small box, as the lightcone contribution is relatively small. However, in our case it would lead to a significant bias of the measured optical depth from other structures along the same line of sight.

The kSZ signal at the position of individual clusters also receives a lightcone contribution, but when averaging over many clusters the latter averages to zero because of the velocity weighting in eq. 2. Also, in the context of the pairwise kSZ measurement, we do not require the optical depth of any individual cluster, but only the mean $\overline{\tau}$ as a function of mass and redshift.

We therefore measure $\overline{\tau}$ from the kSZ map as follows: (1) For every cluster, we apply the adaptive AP filter with $\theta_A = \theta_{vir}$ to the kSZ map to measure $\langle T_{kSZ} \rangle_{vir}$. (2) In every redshift slice, we bin the clusters in 10 logarithmically spaced mass bins (here one could equally well bin by a mass proxy, or use a different number of bins). (3) In every mass bin, we fit a linear relation between $\langle T_{kSZ} \rangle_{vir}$ and the cluster line-of sight velocity v_{los}. From the slope of this relation we determine $\overline{\langle \tau \rangle}_{vir}$ and its associated uncertainty via eq. 2; an example for one redshift and mass bin is shown in Fig. 7. This procedure, which is inspired by the velocity correlation method for kSZ detections, by construction yields the correct *effective* optical depth of the cluster sample in the respective bin. We note, however, that it is not a priori clear that this is also the correct quantity to use in eq. 1 for the *pairwise* kSZ measurement: as mentioned in Sec. 1 above, internal gas motions or correlations between velocity and optical could cause a bias.

We have verified that the optical depth measured as described above is closely related to the 'true' cylindrical gas mass computed directly from the simulation particle data. The AP estimate is, however, on average $\simeq 25\%$ lower than the true gas mass within the virial radius. This bias arises because clusters are no perfect circles in projection and also do not have a sharp edge at R_{vir}. The AP estimate subtracts contributions from $\theta_{vir} < \theta < \sqrt{2}\theta_{vir}$ from the signal

within θ_{vir}, thus reducing the measured gas mass. As expected, this bias disappears when using the simple average-filter without background subtraction instead. Therefore this comparison also serves as a consistency check for our measurement of the optical depth. For a further discussion see Appendix B.

3.4 y-τ scaling relation

Following B16, we model the y-τ relation as

$$\ln \overline{\tau} = \ln \overline{\tau}_0 + \alpha \ln \frac{\overline{y}}{\overline{y}_0} , \tag{13}$$

where we have set the normalization constant to $\overline{y}_0 = 10^{-6}$. This is a typical value for the aperture-averaged Compton-y parameter for the clusters in our sample, so that $\overline{\tau}_0$ is also representative for the typical aperture-averaged optical depth.[6]

Using the binned $\overline{\tau}$ estimates and the $\overline{y}$ computed in the same bins, we then fit for α and $\ln \overline{\tau}_0$ using weighted orthogonal distance regression[7]. We repeat this procedure in every redshift slice, and show an example for two slices in Fig. 8. The resulting fit parameters are reported in Table 2. We have also included the off-diagonal element of the correlation matrix $\mathrm{Corr}(\alpha, \ln \overline{\tau}_0) = C_{\alpha, \ln \overline{\tau}_0}/(\sigma_\alpha \sigma_{\ln \overline{\tau}_0})$, where $C_{\alpha, \ln \overline{\tau}_0}$ is the parameter covariance obtained from the fit.

We note that while there is little change in the normalization $\ln \overline{\tau}_0$, the slope evolves from $\alpha \simeq 0.4$ at low z to $\alpha \simeq 0.6$ at high z. It is instructive to compare these values to the expectation assuming self-similarity (Kaiser 1986). In this case one would expect $\overline{y} \propto Y/\theta_{\mathrm{vir}}^2 \propto M^{5/3}/M^{2/3} = M$ for the average Compton-y parameter, and similarly $\overline{\tau} \propto \mathcal{T}/\theta_{\mathrm{vir}}^2 \propto M/M^{2/3} = M^{1/3}$ (with Y and $\mathcal{T}$ being the Compton-y parameter and optical depth integrated over the aperture). The self-similar expectation would therefore be $\overline{\tau} \propto \overline{y}^{1/3}$. At low redshift we measure an exponent that is relatively close to this value, while at higher redshifts we find a significantly steeper relation.

We have also computed the power-law exponent of the $Y - M$ and $\mathcal{T} - M$ relations; here we use the integrated quantities to avoid an impact of the changing angular diameter distance on the scaling relations. We obtain $Y \propto M^{1.72 \pm 0.01}$ and $\mathcal{T} \propto M^{1.09 \pm 0.03}$ in the lowest redshift bin, which is again close to the self-similar expectation ($Y \propto M^{5/3}$, $\mathcal{T} \propto M$). Both scaling relations steepen towards higher redshift, but the trend is stronger in the $\mathcal{T} - M$ relation, leading to the observed steepening in the $\overline{\tau}$-$\overline{y}$ relation. A possible physical explanation for these trends might be the impact of AGN feedback breaking self-similarity at higher redshifts. [8]

Provided a measurement of the average tSZ signal of a cluster sample, eq. 13 can now be used to predict the optical depth within the same aperture. We compute the predictions for $\overline{\tau}$ separately for all redshift bins in our sample and also report them in Table 2. We will later use these values to convert our pairwise kSZ measurement into an estimate for the mean pairwise velocity. Propagating the statistical uncertainty from the fit and the $\overline{y}$ measurement, the
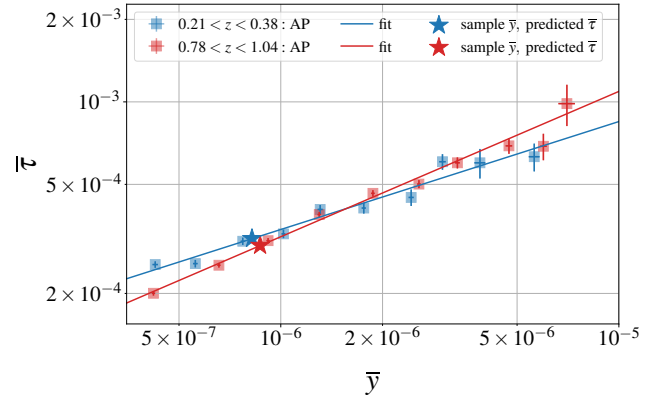
---

[6] We will omit the $\langle . \rangle_{\mathrm{vir}}$ unless there is a potential ambiguity.
[7] https://docs.scipy.org/doc/scipy/reference/odr.html
[8] We note, however, that the subtraction of signal from the cluster outskirts during the AP filtering (see Appendix B) could also have a small impact on the exponent of these relations.

Figure 8. $\overline{y}$-$\overline{\tau}$ scaling relation: We show here the scaling relation for two redshift slices as an example. The square points with error bars denote the individual mass bins of the respective slice; the solid line is the scaling relation fit to them. The position of the asterisk shows the average $\overline{y}$ across all clusters in the slice, and the corresponding $\overline{\tau}$ predicted from the scaling relation.

relative error on the predicted $\overline{\tau}$ is given by

$$\frac{\sigma_{\overline{\tau}}}{\overline{\tau}} = \left[\sigma_{\ln \overline{\tau}_0}^2 + 2 \ln\left(\frac{\overline{y}}{\overline{y}_0}\right) C_{\alpha, \ln \overline{\tau}_0} + \left(\ln \frac{\overline{y}}{\overline{y}_0}\right)^2 \sigma_\alpha^2 + \alpha^2 \left(\frac{\sigma_{\overline{y}}}{\overline{y}}\right)^2 \right]^{1/2} . \tag{14}$$

In the case of a perfectly clean y-map the fractional uncertainty is only 1 to 2% (see Table 2), well below the systematic uncertainty introduced by the sub-grid feedback models used in the simulation (see Sec. 4.3 below for a further discussion). Applied to real data the uncertainty of the $\overline{y}$-measurement would propagate into the prediction for $\overline{\tau}$.

3.5   Pairwise estimator

We use the estimator for the mean pairwise velocity derived by Ferreira et al. (1999),

$$\hat{v}_{12}(r) = \frac{\sum_{i<j,r} (\hat{\mathbf{r}}_i \cdot \mathbf{v}_i - \hat{\mathbf{r}}_j \cdot \mathbf{v}_j) \, c_{ij}}{\sum_{i<j,r} c_{ij}^2} . \tag{15}$$

Here the weights are given by

$$c_{ij} = \hat{\mathbf{r}}_{ij} \cdot \frac{\hat{\mathbf{r}}_i + \hat{\mathbf{r}}_j}{2} \quad \text{with} \quad \mathbf{r}_{ij} \equiv \mathbf{r}_i - \mathbf{r}_j , \quad |\mathbf{r}_{ij}| = r . \tag{16}$$

As the kSZ effect provides a proxy for the line-of-sight velocity (see eq. 2), the same estimator can be applied to kSZ temperature maps (Hand et al. 2012):

$$\hat{T}_{\mathrm{pkSZ}}(r) = -\frac{\sum_{i<j,r} \left[T(\hat{\mathbf{n}}_i) - T(\hat{\mathbf{n}}_j) \right] c_{ij}}{\sum_{i<j,r} c_{ij}^2} . \tag{17}$$

Here we use the same AP-filtered kSZ temperatures as before.

Comparing the estimators for v_{12} and T_{pkSZ} (eqs. 15 and 17), it becomes apparent why eq. 1 is an approximation whose accuracy needs to be tested. Schematically, we have

$$-\langle T_1 - T_2 \rangle_c \simeq \frac{T_{\mathrm{CMB}}}{c} \left\langle \tau_1 v_1^{\mathrm{los}} - \tau_2 v_2^{\mathrm{los}} \right\rangle_c$$
$$\simeq \frac{T_{\mathrm{CMB}}}{c} \overline{\tau} \left\langle v_1^{\mathrm{los}} - v_2^{\mathrm{los}} \right\rangle_c = \overline{\tau} \frac{T_{\mathrm{CMB}}}{c} v_{12} , \tag{18}$$

Parameter	$0.21 < z < 0.38$	$0.38 < z < 0.57$	$0.57 < z < 0.78$	$0.78 < z < 1.04$	$1.04 < z < 1.32$
α	0.39 ± 0.03	0.40 ± 0.01	0.46 ± 0.01	0.53 ± 0.02	0.59 ± 0.02
$\ln \overline{\tau}_0$	-7.98 ± 0.02	-7.94 ± 0.01	-7.98 ± 0.01	-8.04 ± 0.01	-8.13 ± 0.01
$\mathrm{Corr}(\alpha, \ln \overline{\tau}_0)$	0.22	0.10	-0.01	0.00	0.07
χ^2/dof	2.06	0.42	0.66	1.74	0.98
$\overline{y}$	8.22×10^{-7}	8.94×10^{-7}	9.22×10^{-7}	8.69×10^{-7}	7.67×10^{-7}
predicted $\overline{\tau}$	3.17×10^{-4}	3.42×10^{-4}	3.30×10^{-4}	2.99×10^{-4}	2.52×10^{-4}
$\sigma_{\overline{\tau}}/\overline{\tau}$	2%	1%	1%	1%	2%

Table 2. Parameters of the $\overline{\tau}$-$\overline{y}$ scaling relation: We show here the results from the fit together with the mean $\overline{y}$ and predicted $\overline{\tau}$ in every redshift bin. While the first and fourth redshift slice show a somewhat high χ^2 when fitting the scaling relation, the overall χ^2 is acceptable ($\chi^2_{\mathrm{all-z}} = 47$ for 40 degrees of freedom, probability to exceed of 21%).

where we have used the shorthand $\langle ... \rangle_c$ for the estimator of eqs. 15 and 17. The first approximate equality assumes that internal cluster motions do not introduce a bias to the signal. The second step assumes that there is no strong correlation between optical depth and velocity.

We follow previous studies (e.g. Hand et al. 2012; Planck Collaboration 2016a) and subtract the mean temperature as a function of redshift from the kSZ temperature data, i.e.

$$T_i^{\mathrm{corr}} = T_i - \overline{T}(z_i) = T_i - \frac{\sum_j T_j\, G(z_i, z_j, \Sigma_z)}{\sum_j G(z_i, z_j, \Sigma_z)}, \qquad (19)$$

where $G(z_i, z_j, \Sigma_z) = \exp\left[-0.5(z_i - z_j)^2/\Sigma_z^2\right]$. We set $\Sigma_z = 0.01$ to obtain a smoothly varying mean temperature. Furthermore, we apply the same correction to the line-of-sight velocities in the halo catalogue. This is necessary because otherwise large-scale velocity modes within a finite slice through the simulation can cause a bias to the signal on large scales. We then apply this estimator in 20 separation bins linearly spaced between 0 and 300 Mpc.

We further estimate the uncertainties on the pairwise kSZ measurement by bootstrap resampling from the cluster catalogue. Having created N_{BS} bootstrap realisations by drawing with replacement from the catalogue, the covariance matrix is given by

$$\hat{C}_{ij}^{\mathrm{BS}} = (N_{\mathrm{BS}} - 1)^{-1} \sum_{\alpha=1}^{N_{\mathrm{BS}}} (\hat{T}_i^\alpha - \overline{T}_i)(\hat{T}_j^\alpha - \overline{T}_j). \qquad (20)$$

Here $\hat{T}_i^\alpha$ is the pairwise signal in separation bin i and bootstrap realisation α, and $\overline{T}_i$ is its mean over all realisations. We use $N_{\mathrm{BS}} = 2000$ resamples; our covariance is stable against a further increase.[9] When using the inverse covariance matrix C^{-1}, we include the correction factor by Hartlap et al. (2007) to account for the fact that $(C^{\mathrm{BS}})^{-1}$ is a biased estimator of C^{-1}.

For visualisation purposes, we further define the correlation matrix $R_{ij} = C_{ij}/\sqrt{C_{ii}C_{jj}}$ (no sum over repeated indices) and show an example for the central redshift slice in Fig. 9. For separations $r \gtrsim 100$ Mpc there are significant correlations between adjacent separation bins.

3.6 Pairwise velocity

We convert the pairwise kSZ signal into an estimate of the mean pairwise velocity, v_{12}^{kSZ}, via eq. 1. Its covariance matrix is given by

---

[9] We have also computed the covariance from jackknife resamples and find good agreement between the two estimates. For further discussion of covariance estimates for the pairwise kSZ measurement see Soergel et al. (2016) and De Bernardis et al. (2017).
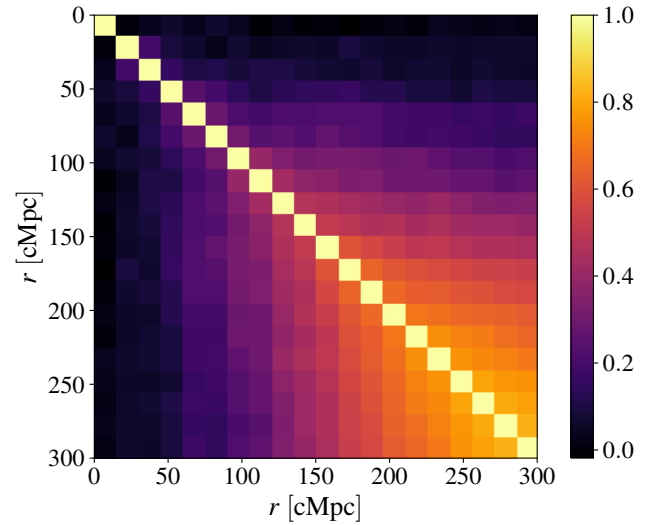
Figure 9. Correlation matrix of the pairwise kSZ measurement in the redshift bin $0.57 < z < 0.78$ as estimated from bootstrap resampling from the catalogue (eq. 20).

$$C_{ij}^{v_{12}} = C_{ij}^{\mathrm{BS}} \left(\frac{c}{\overline{\tau} T_{\mathrm{CMB}}}\right)^2 + \left(\frac{\sigma_{\overline{\tau}}}{\overline{\tau}}\right)^2 v_{12,i}^{\mathrm{kSZ}} v_{12,j}^{\mathrm{kSZ}} \qquad (21)$$

where the second term propagates the uncertainty in the estimate of $\overline{\tau}$. Because we are comparing within the same simulation, we do not include the systematic uncertainty due to the sub-grid feedback models (see Sec. 4.3 below) into $\sigma_{\overline{\tau}}/\overline{\tau}$ here. It should, however, be included when using the scaling relation on real data.

We finally assess how well we recover the true pairwise velocity as measured directly from the halo catalogue. Given a measured data vector $\hat{\mathbf{s}}$ with inverse covariance matrix C_s^{-1} and a theoretical model $\mathbf{s}_{\mathrm{th}}$, we define

$$\chi_a^2 \equiv (\hat{\mathbf{s}} - a\mathbf{s}_{\mathrm{th}})^T C_s^{-1} (\hat{\mathbf{s}} - a\mathbf{s}_{\mathrm{th}}). \qquad (22)$$

The best-fitting value of a, its uncertainty, and the statistical significance are then given by

$$a = \frac{\hat{\mathbf{s}}^T C_s^{-1} \mathbf{s}_{\mathrm{th}}}{\mathbf{s}_{\mathrm{th}}^T C_s^{-1} \mathbf{s}_{\mathrm{th}}}, \qquad \sigma_a^2 = \frac{1}{\mathbf{s}_{\mathrm{th}}^T C_s^{-1} \mathbf{s}_{\mathrm{th}}}, \qquad \frac{S}{N} = \frac{a}{\sigma_a}, \qquad (23)$$

respectively. We have defined the amplitude parameter such that $a = 1$ indicates perfect agreement between model and measurement. Using v_{12} measured directly from the halo catalogue as the
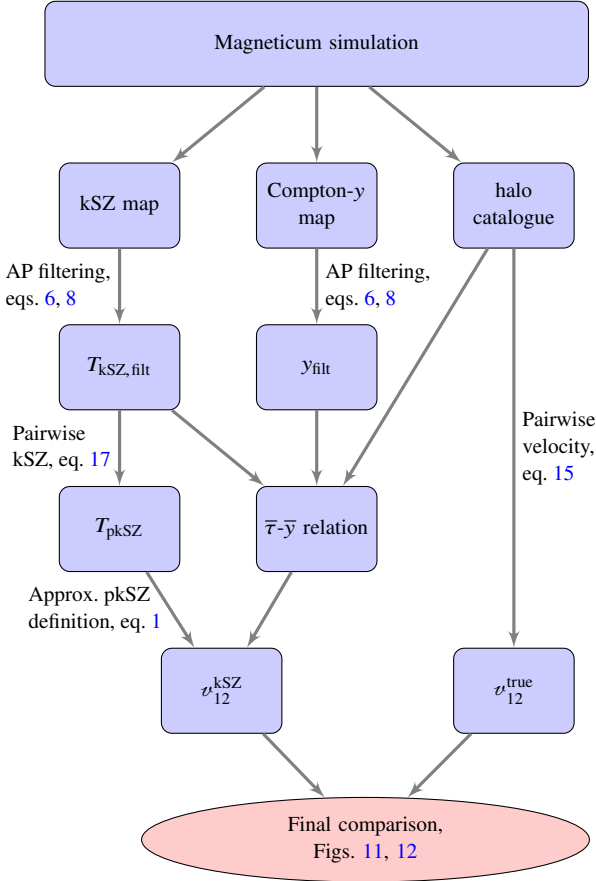
Figure 10. Flowchart summarising the calibration and validation procedure used in this work.

theoretical template, we quantify the agreement between recovered and true mean pairwise velocity via eq. 23. [10]

4   RESULTS AND DISCUSSION

4.1   Pairwise kSZ vs. pairwise velocity

The underlying assumption of using the pairwise kSZ signal as a probe of cosmology is the simple multiplicative relation given by eq. 1. Having established the τ-y scaling relation and the pairwise kSZ estimate, we can now test whether this assumption holds at the high precision required by future surveys.

We compare the estimate of v_{12} from the pairwise kSZ signal (eq. 17) and the τ-y scaling relation to the result obtained directly from the halo catalogue (eq. 15). An overview of the various steps involved in this comparison is given in Fig. 10. Its results are shown in Fig. 11, where we have also included the amplitude fits and statistical significance as computed from eq. 23. We find that the pairwise kSZ signal combined with the τ-y scaling relation yields an accurate estimate of the true mean pairwise velocity.

---

[10]   If instead we want to be agnostic about the expected shape of the signal, we define $\chi^2_{\text{null}} \equiv \hat{\mathbf{s}}^T C_s^{-1} \hat{\mathbf{s}}$. We then convert the associated probability to exceed (PTE) of the χ^2-distribution with 20 degrees of freedom to a significance in standard deviations via the standard normal distribution. In the limit of high S/N (as it is the case for our kSZ only-measurement) the two approaches yield very similar answers.
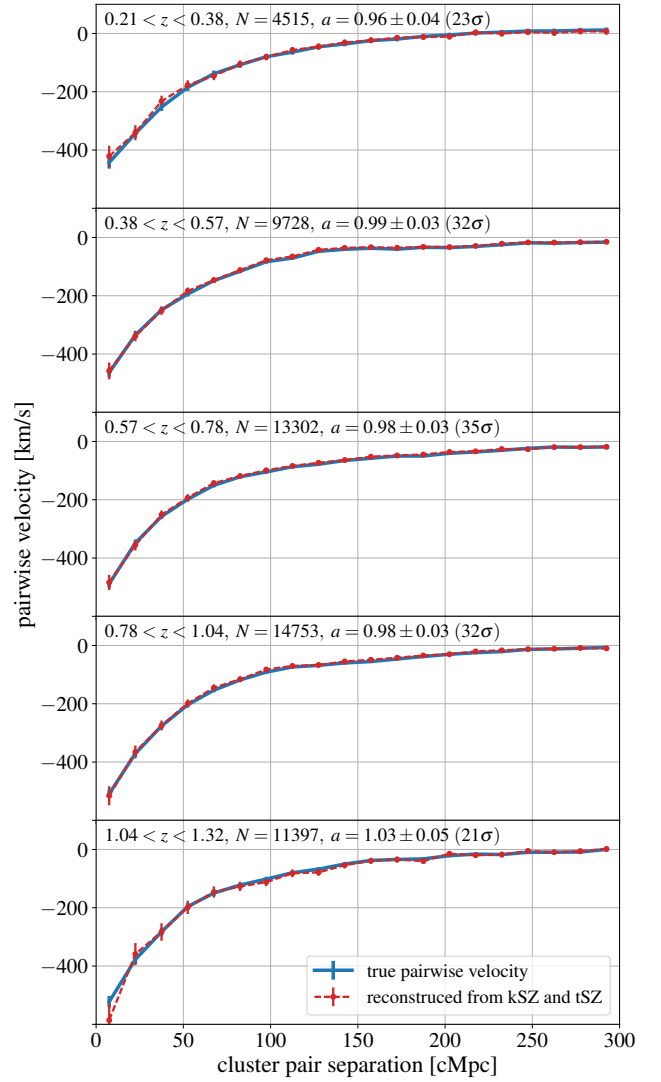

Figure 11. Mean pairwise velocity: We show here v_{12}^{kSZ} (obtained from the pairwise kSZ signal and the y-τ scaling relation) compared to the true values computed directly from the halo catalogue. The error bars on v_{12}^{kSZ} include the statistical errors of the scaling relation, but not the systematic uncertainty due to sub-grid feedback models (see Secs. 3.4 and 4.3). The individual panels show the signal in the different redshift bins. The number of clusters in every bin is given in the respective panel; we have also included the best fitting amplitude and statistical significance (see Sec. 3.6).

The amplitude of the recovered signal is consistent with unity within the statistical uncertainties in all redshift bins. The significances range between 21σ in the highest redshift bin ($1.04 < z < 1.32$) and 35σ in the central bin ($0.57 < z < 0.78$). As we have assumed a perfect kSZ map and a catalogue containing every cluster with $M_{500c} > 3 \cdot 10^{13}\ h^{-1} M_\odot$, these numbers are higher than more elaborate forecasts for future experiments (e.g. Flender et al. 2016). They do, however, highlight that there is a very significant pairwise kSZ signal, especially when pushing down towards lower mass limits.

We further show the ratio between v_{12} recovered from the pairwise kSZ and the true values in Fig 12. In all redshift bins, and at all scales $r \lesssim 150$ Mpc, the differences between the recovered and true v_{12} are well below 10%. Finally, the difference
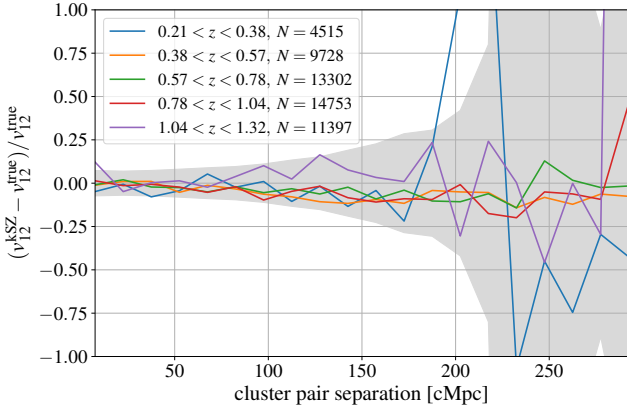
Figure 12. Fractional difference between the mean pairwise velocity recovered from the pairwise kSZ signal and the true values. For reference, the grey shaded band shows the fractional statistical uncertainty on v_{12}^{kSZ} as a function of scale (averaged over all five redshift bins). The increase in fractional error towards large separations is a result of v_{12} going towards zero at large r.

between true and recovered signal is also well below the statistical uncertainties of the pairwise kSZ measurements. This demonstrates that the simple scaling of eq. 1 is indeed sufficient, and that internal cluster motions and/or correlations between velocity and optical depth do not have a strong impact on the pairwise kSZ signal. Furthermore, it shows that the y-τ scaling relation can be used to predict the correct optical depth to be used in eq. 1. Overall, our findings demonstrate that future detections of the pairwise kSZ signal can indeed be used as a probe of cosmology.

4.2 Observational prospects

In the above, we have shown that under idealised circumstances the pairwise kSZ signal combined with the y-τ scaling relation can yield an unbiased estimate of the mean pairwise velocity. Here we now discuss whether the inevitable non-idealities of real data affect this conclusion.

4.2.1 Measurements from realistic CMB data

For measuring the average Compton-y parameter and the pairwise kSZ signal, we have used tSZ- and kSZ-only maps, which are of course not readily available from a real CMB experiment. Thanks to its characteristic multi-frequency signature, however, the tSZ signal can be extracted from multi-frequency CMB data relatively easily: one can either construct a y-map through appropriate linear combination of different bands (e.g. Hill & Spergel 2014; Planck Collaboration 2016c), or combine measurements at multiple frequencies to estimate the tSZ signal of every cluster from a fit to the SED (e.g. Soergel et al. 2016). Therefore we do not expect any bias to the measurement of y when real data including primary CMB, noise, and foregrounds are considered. The kSZ signal, on the other hand, is lacking this distinctive frequency signature, so it cannot be extracted with multi-frequency cleaning techniques. Therefore we have to rely on the differential structure of the pairwise estimator to remove all contributions that do not depend on cluster pair separation; this includes thermal SZ, primary CMB, instrumental noise, and foregrounds such as radio and infrared galaxies.

We have repeated our estimate of the pairwise kSZ signal from a combined kSZ+tSZ map at 150 GHz. To preclude any biases from the large tSZ signal of high-mass clusters (e.g. Flender et al. 2016; Soergel et al. 2016), here we remove all clusters with $M_{500c} > 10^{14}\ h^{-1} M_{\odot}$ from the sample. Thanks to the steepness of the halo mass function and the pairwise nature of our signal, this has only a very small impact on the overall signal-to-noise ratio. We are still able to reconstruct an unbiased estimate of the mean pairwise velocity from this combined kSZ+tSZ map, but the significance is roughly halved: we find $a = \{1.01\pm0.09, 1.03\pm0.06, 0.97\pm 0.06, 1.03\pm0.07, 1.09\pm0.09\}$ in the five redshift slices. Other potential strategies for precluding bias from tSZ and mitigating this loss of signal-to-noise are creating a tSZ-free CMB map by appropriate linear combination, or alternatively working at 217 GHz where the tSZ does not contribute. Which of these strategies is going to recover most of the signal depends on the detailed properties of both the CMB data and the cluster catalogue.

We have also computed the pairwise kSZ signal from a simulated 150 GHz map including kSZ and a Gaussian realization of primary CMB, foregrounds, and instrumental noise. In particular, we compute the CMB power spectrum with CAMB (Lewis et al. 2000), model radio and infrared galaxies according to the best-fitting power spectra from George et al. (2015), and assume an instrumental noise level of 7 μK arcmin (representative of AdvACT-Pol, Calabrese et al. 2014). Again, we recover an unbiased estimate of the mean pairwise velocity, but at significantly reduced signal-to-noise: we find $S/N \simeq \{2, 4, 7, 3, 2\}$ for the five redshift bins. The estimated S/N is, however, based on only $\simeq 1600$ deg^2, or a sky coverage of $\simeq 4\%$. For an experiment with larger sky coverage, these numbers should be rescaled by a factor of $\simeq (f_{\mathrm{sky}}/0.04)^{1/2}$. In the case of AdvActPol $\times$ DESI (Levi et al. 2013) we therefore expect an approximately three times higher signal-to-noise ratio.

It is worth noting that at these low noise levels the power on cluster scales is already becoming dominated by foregrounds (as opposed to instrumental noise for ACT and SPT-SZ). Some of these foregrounds, most notably emission from radio and infrared galaxies, are correlated with the kSZ signal because a fraction of these galaxies resides in group- or cluster-sized haloes. At frequencies below 217 GHz (where the tSZ contribution is negative), they will additionally anti-correlate with the tSZ signal, so that the contributions from these contaminants mix and partially cancel in a nontrivial way. Modelling them as Gaussian random fields with their measured power spectra is therefore clearly insufficient. Instead, a population of radio- and infrared galaxies has to be extracted from the simulation (e.g. Davé et al. 2010; Fontanot & Somerville 2011; Hirschmann et al. 2014).

4.2.2 Other observational effects

Cluster properties: We have assumed that the angular size of every cluster is known, which is of course not the case for real data. However, as argued above, a mass-observable relation provides an estimate for the average radius of clusters of a given mass and redshift. We have tested that binning clusters by their angular size and repeating the AP procedure with an aperture given by the binned radii does not change our results significantly.

Miscentering: A further potential source of systematic uncertainty are offsets between the cluster centre and the peak of the SZ signal. If they are of physical origin, as in the case of unrelaxed or merging clusters, their effects are captured in our hydrodynamical simulations and therefore in our scaling relation. If, on the other

hand, they are caused by imperfections in the cluster finding algorithm (such as mis-identification of the central galaxy in optical cluster finders), they will introduce a bias on both the average y and the measured pairwise kSZ signal (Flender et al. 2016; Soergel et al. 2016; Calafut et al. 2017). A more detailed investigation of this latter issue would, however, require a full simulation of observational cluster finding tailored to a particular experiment.

4.3 Systematic uncertainties from sub-grid physics

Our simulation includes prescriptions for the relevant feedback processes, which allow to properly reproduce various observational properties of the ICM (see Sec. 2.2). There are, however, still a number of uncertainties associated with these sub-grid models and their implementation. As extreme examples, various authors in the past compared ICM properties of simulations with and without AGN feedback (e.g. Puchwein et al. 2008; Planelles et al. 2013, 2014, 2017, B16). In particular, B16 repeated the calibration of the y-τ scaling relation for a simulation run with and without AGN feedback, finding 6-8% difference at their default aperture of $1.3'$ and a decreasing trend towards larger apertures. This should be taken as a very conservative upper bound for the systematic uncertainty on the y-τ relation.

Recent simulations for the first time match various observed ICM properties: they are able to reproduce cool-core and non-cool-core clusters (Rasia et al. 2015; Planelles et al. 2017), as well as matching the observed chemical footprint (Biffi et al. 2017; Dolag et al. 2017). Changing sub-grid models without losing the current level of agreement between simulations and observations is no longer a simple task, and is even more complicated for the large simulation boxes that we consider. Therefore we adopt the values of B16 as a conservative estimate of the systematic uncertainty in the scaling relation. In reality, however, these errors will likely be smaller considering variations in current simulations. As already noted in B16, this systematic uncertainty is nonetheless larger than the statistical errors on the scaling relation. The calibration of the y-τ relation on simulations is therefore currently limited by the unknown real uncertainty on the feedback prescriptions.

It is worth noting that currently the pairwise kSZ signal has only been detected at the 4σ level (Soergel et al. 2016; De Bernardis et al. 2017). This number is expected to increase significantly with data from the second- and third-generation receivers at ACT and SPT (e.g. Flender et al. 2016), so that eventually the statistical uncertainties are going to become comparable to the current systematic uncertainty on the scaling relation. However, we expect that future data and/or more advanced analyses going beyond the power spectrum are also going to help with further improving the feedback models in the simulations. For example, measurements of the bispectrum of secondary CMB anisotropies (e.g. Crawford et al. 2014; Coulton et al. 2017) improve our ability to separate the SZ signal from foregrounds, and might also provide additional constraints on feedback processes. Combining future tSZ and kSZ data also enables improved constraints on cluster thermodynamics and feedback efficiencies (Battaglia et al. 2017).

Another possibility to reduce the dependency of the SZ signal on baryonic physics would be to excise the core of the clusters, similar to what is done in X-ray analyses. This would, however, require data with significantly higher resolution. This could be achieved from interferometric observations, which are, however, observationally much more expensive.

4.4 Implications for other kSZ detection techniques

In the above we have focused exclusively on the real-space pairwise estimator, as it is a robust technique that has already led to several kSZ detections from different experiments. Here we now discuss the implications of our findings for other techniques.

The Fourier space version of the pairwise estimator derived by Sugiyama et al. (2017b,a) captures the effect of redshift-space distortions on the pairwise kSZ signal by decomposing the signal into multipoles, with the dipole approximately corresponding to the standard real-space measurement. In principle, the different k-dependence of the dipole and octopole would allow to marginalize over the amplitude (which depends on the optical depth). In practice, however, the signal-to-noise ratio is completely dominated by the dipole: Sugiyama et al. (2017b) forecast $S/N \simeq 30$ for the dipole from a survey volume of $1\ h^{-3}\mathrm{Gpc}^3$ and for CMB-S4 (Abazajian et al. 2016) noise levels, compared to only $S/N \simeq 3$ for the octopole. Therefore additional information on the amplitude from the y-τ relation would still be valuable to break the degeneracy between optical depth and velocity.

Velocity reconstruction-based techniques (Li et al. 2014; Schaan et al. 2016; Planck Collaboration 2016a) suffer from a similar same degeneracy between velocity and optical depth (e.g. Alonso et al. 2016), so also here the y-τ relation could be a useful tool. The same holds true for estimates of the cluster velocity dispersion from the kSZ (Planck Collaboration 2017).

With future CMB observatories with a larger number of frequency bands, such as CCAT (Woody et al. 2012) or CMB-S4, it might also be possible to isolate the kSZ signal of a larger number of clusters than currently possible. The degeneracy between optical depth and velocity can then be broken by including relativistic corrections to the SZ spectrum and/or X-ray-based temperature priors (Sehgal et al. 2005; Mittal et al. 2017). However, this approach is mostly limited to relatively massive clusters.

Approaches based on smooth fields instead of haloes, such as the 'projected fields' technique by Hill et al. (2016); Ferraro et al. (2016), are sensitive to the free electron fraction instead of the optical depth. Potentially a similar approach (e.g. calibrating a relation to the tSZ power spectrum or bispectrum) could be applied here, but further work is required to study the relation between the different SZ spectra in detail.

5   CONCLUSIONS

The pairwise kSZ signal has significant potential as a probe of cosmology. It could allow for an independent measurement of the parameter combination $Hf\sigma_8^2$, breaking degeneracies between these parameters from other probes of the growth of structure. Realising this potential, however, requires disentangling the cluster optical depth (and all the associated uncertainties on baryonic physics) from the cosmologically interesting mean pairwise velocity.

One promising avenue for this is to calibrate a scaling relation between the Compton-y parameter and the optical depth on hydrodynamical simulations. Given a measurement of the average tSZ signal of a cluster sample, this relation can then be used to predict the average optical depth. Provided that internal cluster motions and/or correlations between velocity and optical depth do not have a significant impact on the signal, we can then recover the mean pairwise velocity from the kSZ signal.

Here we have investigated whether this procedure returns an unbiased estimate of v_{12} at the precision required by the high

signal-to-noise measurements expected from future surveys. For this purpose we have created SZ maps and cluster catalogues from the largest ($L = 2688 \ h^{-1}$Mpc) box of the *Magneticum* simulation suite. Thanks to its large box size, for the first time we have been able to produce SZ maps from hydrodynamical simulations that cover a sky area comparable to current high-resolution CMB experiments.

We have measured the average Compton-y parameter within the virial radius by applying an aperture photometry filter with adaptive size to the y-map. For measuring the optical depth we have applied the same procedure to the kSZ map, and then correlate the AP-filtered values with the cluster line-of-sight velocities. This yields an estimate of the average optical depth $\bar{\tau}$ as a function of mass and redshift. We have then fit a scaling relation between the two quantities, paying particular attention to any potential biases which could arise when applying that relation to SZ measurements from real CMB data.

We have finally computed the pairwise kSZ signal using the same AP estimates as before. From the average $\bar{y}$ in every redshift slice, we have predicted the corresponding average $\bar{\tau}$, and have used it to convert $T_{\rm pkSZ}(r)$ into $v_{12}(r)$. These estimates are then compared to the 'true' values computed from the halo catalogue. We have found excellent agreement between the reconstructed and true mean pairwise velocity. In other words, we have demonstrated that the pairwise kSZ signal yields an unbiased estimate of the cosmologically interesting mean pairwise velocity, and that the degeneracy between velocity and optical depth can be overcome by using the τ-y scaling relation. Therefore the pairwise kSZ effect can indeed be used as a probe of cosmology.

The largest systematic uncertainty associated with our scaling relation are the remaining variations between the sub-grid feedback models implemented in hydrodynamical simulations. While obtaining realistic estimates for the errors in the calibration of the scaling relation based on large cosmological volumes will be a major task for the next generation of simulation campaigns, we have adopted the 6-8% from B16 as a conservative estimate of such systematic uncertainty. Although this is well below the statistical uncertainty of current (and expected near-future) pairwise kSZ detections, eventually the measurements will reach this systematic floor. Therefore, further work on the calibration of feedback models is required to realize the full potential of the pairwise kSZ signal as a cosmological probe.

REFERENCES

Abazajian K. N., et al., 2016, preprint, (arXiv:1610.02743)
Afshordi N., Lin Y.-T., Nagai D., Sanderson A. J. R., 2007, MNRAS, 378, 293
Aghanim N., Górski K. M., Puget J.-L., 2001, A&A, 374, 1
Ahn C. P., et al., 2012, ApJS, 203, 21
Alonso D., Louis T., Bull P., Ferreira P. G., 2016, Phys. Rev. D, 94, 043522
Arnaud M., Pratt G. W., Piffaretti R., Böhringer H., Croston J. H., Pointecouteau E., 2010, A&A, 517, A92
Astropy Collaboration 2013, A&A, 558, A33
Battaglia N., 2016, J. Cosmology Astropart. Phys., 8, 058
Battaglia N., Bond J. R., Pfrommer C., Sievers J. L., 2012, ApJ, 758, 74
Battaglia N., Ferraro S., Schaan E., Spergel D. N., 2017, J. Cosmology Astropart. Phys., 11, 040
Beck A. M., et al., 2016, MNRAS, 455, 2110
Bhattacharya S., Kosowsky A., 2007, ApJ, 659, L83
Bhattacharya S., Kosowsky A., 2008, Phys.Rev., D77, 083004
Biffi V., et al., 2017, MNRAS, 468, 531
Birkinshaw M., 1999, Phys.Rept., 310, 97
Bleem L. E., et al., 2015, ApJS, 216, 27
Bocquet S., Saro A., Dolag K., Mohr J. J., 2016, MNRAS, 456, 2361
Bryan G. L., Norman M. L., 1998, ApJ, 495, 80
Calabrese E., et al., 2014, J. Cosmology Astropart. Phys., 8, 010
Calafut V., Bean R., Yu B., 2017, preprint, (arXiv:1710.01755)
Carlstrom J. E., Holder G. P., Reese E. D., 2002, Ann.Rev.A&A, 40, 643
Chluba J., Mannheim K., 2002, A&A, 396, 419
Cooray A., Chen X., 2002, ApJ, 573, 43
Coulton W. R., et al., 2017, preprint, (arXiv:1711.07879)
Crawford T. M., et al., 2014, ApJ, 784, 143
Dalcin L., Bradshaw R., Smith K., Citro C., Behnel S., Seljebotn D. S., 2010, Computing in Science & Engineering, 13, 31
Dark Energy Survey Collaboration 2016, MNRAS, 460, 1270
Das S., Hajian A., Spergel D. N., 2009, Phys. Rev. D, 79, 083008
Davé R., Finlator K., Oppenheimer B. D., Fardal M., Katz N., Kereš D., Weinberg D. H., 2010, MNRAS, 404, 1355
De Bernardis F., et al., 2017, J. Cosmology Astropart. Phys., 3, 008
Diaferio A., Sunyaev R. A., Nusser A., 2000, ApJ, 533, L71
Diaferio A., et al., 2005, MNRAS, 356, 1477
Diego J. M., Partridge B., 2010, MNRAS, 402, 1179
Dolag K., Sunyaev R., 2013, MNRAS, 432, 1600
Dolag K., Hansen F. K., Roncarelli M., Moscardini L., 2005, MNRAS, 363, 29
Dolag K., Borgani S., Murante G., Springel V., 2009, MNRAS, 399, 497
Dolag K., Komatsu E., Sunyaev R., 2016, MNRAS, 463, 1797
Dolag K., Mevius E., Remus R.-S., 2017, Galaxies, 5, 35
Dunkley J., Calabrese E., Sievers J., Addison G., Battaglia N., et al., 2013, J. Cosmology Astropart. Phys., 1307, 025
Erler J., Basu K., Chluba J., Bertoldi F., 2017, preprint, (arXiv:1709.01187)
Ferraro S., Hill J. C., Battaglia N., Liu J., Spergel D. N., 2016, Phys. Rev. D, 94, 123526
Ferreira P., Juszkiewicz R., Feldman H., Davis M., Jaffe A. H., 1999, ApJ, 515, L1
Flender S., Bleem L., Finkel H., Habib S., Heitmann K., Holder G., 2016, ApJ, 823, 98

Flender S., Nagai D., McDonald M., 2017, ApJ, 837, 124

Fontanot F., Somerville R. S., 2011, MNRAS, 416, 2962

George E., Reichardt C., Aird K., Benson B., Bleem L., et al., 2015, ApJ, 799, 177

Gupta N., Saro A., Mohr J. J., Dolag K., Liu J., 2017, MNRAS, 469, 3069

Haehnelt M. G., Tegmark M., 1996, MNRAS, 279, 545

Hajian A., Battaglia N., Spergel D. N., Bond J. R., Pfrommer C., Sievers J. L., 2013, J. Cosmology Astropart. Phys., 11, 064

Hand N., Addison G. E., Aubourg E., Battaglia N., Battistelli E. S., et al., 2012, Phys.Rev.Lett., 109, 041101

Hartlap J., Simon P., Schneider P., 2007, A&A, 464, 399

Hasselfield M., Hilton M., Marriage T. A., Addison G. E., et al., 2013, J. Cosmology Astropart. Phys., 1307, 008

Hernández-Monteagudo C., Ma Y.-Z., Kitaura F. S., Wang W., Génova-Santos R., Macías-Pérez J., Herranz D., 2015, Physical Review Letters, 115, 191301

Hill J. C., Spergel D. N., 2014, J. Cosmology Astropart. Phys., 2, 030

Hill J. C., Ferraro S., Battaglia N., Liu J., Spergel D. N., 2016, Physical Review Letters, 117, 051301

Hirschmann M., Dolag K., Saro A., Bachmann L., Borgani S., Burkert A., 2014, MNRAS, 442, 2304

Kaiser N., 1986, MNRAS, 222, 323

Keisler R., Schmidt F., 2013, ApJ, 765, L32

Komatsu E., et al., 2011, ApJS, 192, 18

Levi M., et al., 2013, preprint, (arXiv:1308.0847)

Lewis A., Challinor A., Lasenby A., 2000, ApJ, 538, 473

Li M., Angulo R. E., White S. D. M., Jasche J., 2014, MNRAS, 443, 2311

Li Y.-C., Ma Y.-Z., Remazeilles M., Moodley K., 2017, preprint, (arXiv:1710.10876)

Lueker M., Reichardt C., Schaffer K., Zahn O., Ade P., et al., 2010, ApJ, 719, 1045

Ma Y.-Z., Gong G.-D., Sui N., He P., 2017, preprint, (arXiv:1711.08756)

McCarthy I. G., Le Brun A. M. C., Schaye J., Holder G. P., 2014, MNRAS, 440, 3645

Melchior P., et al., 2017, MNRAS, 469, 4899

Mittal A., de Bernardis F., Niemack M. D., 2017, preprint, (arXiv:1708.06365)

Mueller E.-M., de Bernardis F., Bean R., Niemack M. D., 2015a, Phys. Rev. D, 92, 063501

Mueller E.-M., de Bernardis F., Bean R., Niemack M. D., 2015b, ApJ, 808, 47

Nagai D., Kravtsov A. V., Kosowsky A., 2003, ApJ, 587, 524

Nelson K., Lau E. T., Nagai D., 2014, ApJ, 792, 25

Park H., Alvarez M. A., Bond J. R., 2017, preprint, (arXiv:1710.02792)

Plagge T., et al., 2010, ApJ, 716, 1118

Planck Collaboration 2011, A&A, 536, A12

Planck Collaboration 2013a, A&A, 550, A131

Planck Collaboration 2013b, A&A, 557, A52

Planck Collaboration 2016a, A&A, 586, A140

Planck Collaboration 2016b, A&A, 594, A13

Planck Collaboration 2016c, A&A, 594, A22

Planck Collaboration 2016d, A&A, 594, A27

Planck Collaboration 2017, preprint, (arXiv:1707.00132)

Planelles S., Borgani S., Dolag K., Ettori S., Fabjan D., Murante G., Tornatore L., 2013, MNRAS, 431, 1487

Planelles S., Borgani S., Fabjan D., Killedar M., Murante G., Granato G. L., Ragone-Figueroa C., Dolag K., 2014, MNRAS, 438, 195

Planelles S., et al., 2017, MNRAS, 467, 3827

Pollina G., Hamaus N., Dolag K., Weller J., Baldi M., Moscardini L., 2017, MNRAS, 469, 787

Puchwein E., Sijacki D., Springel V., 2008, ApJ, 687, L53

Rasia E., et al., 2015, ApJ, 813, L17

Remus R.-S., Dolag K., Hoffmann T., 2017a, Galaxies, 5, 49

Remus R.-S., Dolag K., Naab T., Burkert A., Hirschmann M., Hoffmann T. L., Johansson P. H., 2017b, MNRAS, 464, 3742

Rephaeli Y., Lahav O., 1991, ApJ, 372, 21

Saro A., et al., 2014, MNRAS, 440, 2610

Saro A., et al., 2015, MNRAS, 454, 2305

Saro A., et al., 2017, MNRAS, 468, 3347

Sayers J., Mroczkowski T., Zemcov M., Korngut P., Bock J., et al., 2013, ApJ, 778, 52

Schaan E., et al., 2016, Phys. Rev. D, 93, 082002

Sehgal N., Kosowsky A., Holder G., 2005, ApJ, 635, 22

Sheth R. K., Diaferio A., Hui L., Scoccimarro R., 2001, MNRAS, 326, 463

Simet M., McClintock T., Mandelbaum R., Rozo E., Rykoff E., Sheldon E., Wechsler R. H., 2017, MNRAS, 466, 3103

Soergel B., et al., 2016, MNRAS, 461, 3172

Soergel B., Giannantonio T., Efstathiou G., Puchwein E., Sijacki D., 2017, MNRAS, 468, 577

Springel V., 2005, MNRAS, 364, 1105

Springel V., White S. D. M., Tormen G., Kauffmann G., 2001, MNRAS, 328, 726

Steinborn L. K., Dolag K., Comerford J. M., Hirschmann M., Remus R.-S., Teklu A. F., 2016, MNRAS, 458, 1013

Sugiyama N. S., Okumura T., Spergel D. N., 2017a, preprint, (arXiv:1705.07449)

Sugiyama N. S., Okumura T., Spergel D. N., 2017b, J. Cosmology Astropart. Phys., 1, 057

Sunyaev R. A., Zeldovich Y. B., 1970, Ap&SS, 7, 3

Sunyaev R. A., Zeldovich Y. B., 1972, Comments on Astrophysics and Space Physics, 4, 173

Sunyaev R. A., Zeldovich I. B., 1980, MNRAS, 190, 413

Swetz D., Ade P., Amiri M., Appel J., Battistelli E., et al., 2011, ApJS, 194, 41

Teklu A. F., Remus R.-S., Dolag K., Beck A. M., Burkert A., Schmidt A. S., Schulze F., Steinborn L. K., 2015, ApJ, 812, 29

Teklu A. F., Remus R.-S., Dolag K., Burkert A., 2017, MNRAS, 472, 4769

The Dark Energy Survey Collaboration 2005, preprint, (arXiv:astro-ph/0510346)

Woody D., et al., 2012, in Ground-based and Airborne Telescopes IV. p. 84442M, doi:10.1117/12.925229

APPENDIX A: IMPACT OF THE INSTRUMENTAL BEAM

In this appendix we discuss the impact of the instrumental beam on the AP estimates of the optical depth. Intuitively, the instrumental beam broadens the cluster profile, and therefore moves part of the signal from the inner AP disk to the outer ring. As the latter is used for the background subtraction, the beam broadening leads to part of the signal being subtracted as well. Here we develop a simplistic model to estimate the magnitude of this effect.

If the projected electron density profile of a cluster is given by $n_e(\theta)$, its average optical depth after beam-convolution and AP filtering scales as (Sugiyama et al. 2017a)

$$\langle\tau\rangle_A \propto \int \frac{d^2\boldsymbol{\ell}}{(2\pi)^2} \tilde{W}_{AP}(\ell\theta_A) n(\boldsymbol{\ell}) B(\boldsymbol{\ell}), \tag{A1}$$

where $n(\boldsymbol{\ell})$ and $B(\boldsymbol{\ell})$ are the Fourier transforms of the projected electron density and beam profile, respectively. The relative impact of the instrumental beam on the estimate is then given by the ratio $\langle\tau\rangle_A^{\text{no-beam}}/\langle\tau\rangle_A$, where for $\langle\tau\rangle_A^{\text{no-beam}}$ we simply set $B(\boldsymbol{\ell}) = 1$ in eq. A1.

For simplicity we assume that $n_e(\theta)$ is given by a Gaussian profile with $\sigma = 0.5 \times \theta_{\text{vir}}$. This choice predicts that around 15% of the gas mass are outside θ_{vir}, which is broadly in agreement with our findings in Appendix B. As in our main analysis, we use an aperture of $\theta_A = \theta_{\text{vir}}$, and assume an instrumental beam with FWHM = $1.2'$ (representative of high-resolution CMB experiments like ACT and SPT). We note that in this simplistic picture the result only depends on the ratio between beam FWHM and θ_{vir}.

Using $\theta_{\rm vir} = 2'$, which corresponds to the median projected virial radius of our central redshift bin, we find

$$\langle\tau\rangle_A^{\rm no-beam}/\langle\tau\rangle_A \simeq 0.85 \,. \tag{A2}$$

If we use $\theta_{\rm vir} = 1'\,(4')$ instead, the resulting ratios are 0.52 and 0.96, respectively. We therefore see that depending on the angular size of the cluster (and therefore the aperture) the impact of the beam on the AP estimate can be significant.

In Appendix B below we convert our estimates of $\langle\tau\rangle_A$ into a gas mass and compare to the 'true' value measured from the simulation particle data. As part of this comparison, we also quantify the impact of the beam on the AP estimates directly from the simulations, see Fig. B1. Here the beam convolution reduces the AP estimate by 11% (5%) in the lowest (highest) mass bin with $\theta_{\rm vir} \simeq 2'$ $(4')$, broadly in agreement with the simplistic model we derived above.

When estimating the average Compton-y parameter within an aperture we simply replace $n_e(\theta)$ in eq. A1 by $n_e(\theta)T(\theta)$. Crucially, the angular dependences of tSZ and kSZ are different: the tSZ signal is more peaked towards the centre. Therefore, the relative effect of the beam on the two components as calculated above is different. This could therefore have an impact on the slope of the τ-y relation.

In our main analysis we have convolved the SZ maps with an instrumental beam with FWHM = $1.2'$ before estimating the scaling relation. Repeating the calculation above with FWHM = $1'$ and $1.4'$, we have tested that a small mismatch between the assumed and real beam size only affects the results at the level of a few percent, which is below the systematic uncertainty given by the sub-grid feedback models (see Sec. 4.3).

APPENDIX B: RELATION OF THE OPTICAL DEPTH TO THE TRUE GAS MASS

In the main analysis our discussion of the optical depth has focussed on using it in the context of pairwise kSZ measurements. Here we now investigate if the average optical depth can also be used as a probe of the true gas mass of the clusters.

The average optical depth within an aperture θ_A relates to the *cylindrical* gas mass as

$$\begin{aligned}
M_{\rm gas,A}^{\rm cyl} &= \int_{\rm cyl} {\rm d}V\,\rho_{\rm gas} = \frac{d_A^2 \mu_e m_p}{\sigma_T} \int_{\theta_A} {\rm d}\Omega \int {\rm d}l\, n_e \sigma_T \\
&= \frac{\mu_e m_p}{\sigma_T} \pi \,(\theta_A d_A)^2 \,\langle\tau\rangle_A \,,
\end{aligned} \tag{B1}$$

where $\mu_e \simeq 1.14$ is the mean particle weight per electron (assuming primordial abundances) and m_p is the proton mass. This relation provides us with a way of comparing our measurement of the optical depth from the main analysis to the 'true' gas mass in the simulations.

However, computing $M_{\rm gas}^{\rm cyl}$ for all clusters in our large simulation box and for various redshifts and apertures would be computationally unfeasible. Therefore we perform this comparison using the second-largest *Magneticum* simulation box. This 'Box1' has a sidelength of $L = 896\ h^{-1}{\rm Mpc}$ and the same resolution as the larger 'Box0' that we used for the main analysis. Cluster catalogues and SZ maps from this box were produced in the same way as for the large box (albeit with thinner redshift slices), and have already been presented in Saro et al. (2014); Dolag et al. (2016); Gupta et al. (2017).
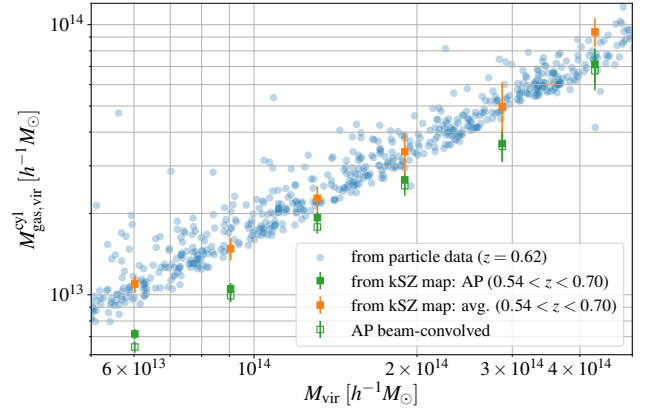

Figure B1. Estimates of the gas mass from the averaged optical depth: We compare here $M_{\rm gas}^{\rm cyl}$ as estimated from the average- and AP-filtered kSZ maps to the 'true' value obtained directly from the simulation particle data. While the main comparison is performed without convolving with the instrumental beam, we also show the effect of including the beam for the AP filter (see Appendix A).

To preclude any bias from the beam convolution (see Appendix A), we perform this comparison using the unconvolved maps. Furthermore, we perform this comparison using a representatively chosen subset of clusters (15 mass bins and 5 redshift bins, 100 randomly chosen clusters per bin). For these objects, we calculate $M_{\rm gas}^{\rm cyl}$ for various apertures directly from the simulation particle data, including particles with up to 10 $h^{-1}{\rm Mpc}$ line-of-sight distance from the cluster centre. We then compare this direct integration to an estimate of the gas mass obtained from our measurements of $\bar\tau$ via eq. B1, both for the average and the AP filter.

We note that the AP filter subtracts contributions in an annulus of $\theta_A < \theta < \sqrt{2}\theta_A$ from the signal within a disk with $\theta < \theta_A$. As clusters are not perfect circles in projection and do not have a sharp edge at any given radius, the AP filter will by construction yield an estimate of the gas mass that is biased low. The level of bias will be largest for small apertures ($\theta_A \lesssim \theta_{500}$) and should decrease when including more of the cluster outskirts ($\theta_A \gtrsim \theta_{\rm vir}$). On the other hand, the gas mass derived from the average-filtered $\bar\tau$ should be a much better estimator of the true cylindrical gas mass.

We show in Fig. B1 an example of the comparison for $z \simeq 0.6$ and $\theta_A = \theta_{\rm vir}$. Here we indeed observe that the AP-estimate of $M_{\rm gas}^{\rm cyl}$ is $\simeq 25\%$ lower than the true value, while the average filter yields the correct estimate of $M_{\rm gas}^{\rm cyl}$. We have repeated this test for various apertures between θ_{500} and $1.5 \times \theta_{\rm vir}$ and obtained the expected trend of decreasing bias of the AP estimate at larger apertures. Furthermore, we have repeated these comparisons for the other redshift bins and have obtained comparable results.

These comparisons also demonstrate that the way of measuring $\bar\tau$ that we describe in Sec. 3.3 above indeed yields the expected results.

This paper has been typeset from a T$_{\rm E}$X/L^{A}T$_{\rm E}$X file prepared by the author.